Mon. Not. R. Astron. Soc. **303,** 367–379 (1999)

Mid-infrared imaging and spectroscopy of the southern H II region RCW 38

Craig H. Smith,[1] Tyler L. Bourke,[1,2⋆] Christopher M. Wright,[3,4] Henrik W. W. Spoon,[4] David K. Aitken,[5] Garry Robinson,[1] John W. V. Storey,[6] Takuya Fujiyoshi,[1] Patrick F. Roche[7] and Thomas Lehmann[8]

[1]*School of Physics, University College, ADFA, UNSW, Canberra, ACT 2600, Australia*
[2]*Harvard–Smithsonian Center for Astrophysics, 60 Garden Street, MS 42, Cambridge, MA 02138, USA*
[3]*Leiden Observatory, Postbus 9513, 2300 RA Leiden, the Netherlands*
[4]*Max-Planck-Institut für extraterrestrische Physik, Postfach 1603, D-85740 Garching, Germany*
[5]*Division of Physical Sciences, University of Hertfordshire, College Lane, Hatfield, Herts AL10 9AB*
[6]*School of Physics, The University of New South Wales, Sydney, NSW 2052, Australia*
[7]*Department of Astrophysics, Oxford University, Keble Road, Oxford OX1 3RH*
[8]*Astrophysical Institute and University Observatory, Schillergäßchen 2, D-07745 Jena, Germany*

Accepted 1998 October 16. Received 1998 August 18; in original form 1998 May 8

ABSTRACT

We present mid-infrared images and an 8–13 μm spectrum of the southern H II region RCW 38. We determine the dust colour temperature from both our spectrum and images at 10 and 20 μm, and deduce the gas excitation from an image in the [S IV] fine-structure line, as well as spectra of the [Ar III], [S IV] and [Ne II] fine-structure lines. Our observations are consistent with a complex of sources associated with the RCW 38 IRS1 region, which represent knots of material in a shell, or ridge, surrounding a cavity of about 0.1 pc in radius, which is itself created by the stellar wind of the hot young source IRS2. The dust temperature does not peak closest to IRS2, but rather along the centre of the ridge, and is remarkably uniform over the extent of our image. From photoionization models for the observed line ratios at IRS1 we deduce a stellar effective temperature and gas density of about 43 000–48 000 K and 10^4 cm^{-3} respectively. Whilst the star, or star cluster, IRS2 is ultimately responsible for the observed thermal and ionic emission, the relatively uniform dust temperature implies that the bulk of the dust heating in the region is provided by resonantly trapped Lyman α photons, rather than direct stellar photons. This then also implies that the dust is depleted with respect to the gas by a factor of at least 100 from its normal interstellar value. The small-scale spatial variations in the continuum emission and temperature can be explained by changes in the density and/or gas-to-dust mass ratio.

Key words: stars: formation – H II regions – ISM: individual: RCW 38 – infrared: ISM: continuum.

1 INTRODUCTION

RCW 38 (Rodgers, Campbell & Whiteoak 1960) is a luminous H II region ($\sim 7 \times 10^5$ L$_\odot$; Furniss, Jennings & Moorwood 1975) located in the region of the Vela supernova remnant and the Gum nebula (Gum 1952, 1956). The reported distance to RCW 38 varies somewhat, but a reasonably consistent value is found amongst Radhakrishnan et al. (1972) of 1.5 kpc, Muzzio (1979) of 1.7 kpc, and Beck, Fisher & Smith (1991) of 1.7±0.9 kpc. In this paper we adopt a distance of 1.7 kpc for RCW 38.

Frogel & Persson (1974, hereafter FP74) produced a 10-μm map of the region with a spatial resolution of 14.5 arcsec, showing the warm dust emission to be spatially extended in a horse-shoe shape over a 1.8 × 1.8 arcmin^2 area. The peak of their map is labelled IRS1, but does not correspond with the bright 2.2-μm source IRS2 that dominates at near-infrared (NIR) wavelengths (FP74). FP74 found IRS1 to be extended on a scale of about 9 arcsec. Epchtein & Turon (1979) mapped a smaller (40 × 40 arcsec^2) region with a spatial resolution of 7 arcsec. They found that the strong 10-μm peak IRS1 resolves into a number of more discrete sources, which they suggested may be due to local heating sources (i.e., a cluster of embedded young stars), or dust opacity variations.

A low-resolution (warm filter) 10-μm spectrum of RCW 38 IRS1 is presented in Persson, Frogel & Aaronson (1976). From simple two-parameter fits to the spectrum they derive a dust temperature of 175 K and a modest absorption optical depth of $\tau_{9.7\mu m} = 0.4$.

From its NIR colours FP74 suggest that IRS2 represents an early

⋆AAO/ATNF Post-doctoral Fellow. Present address: Anglo-Australian Observatory, PO Box 296, Epping, NSW, 1710, Australia.

O star (around O4) or group of stars, suffering 12.8 magnitudes of extinction. As noted by Furniss et al. (1975), the ionizing flux from such a star is more than sufficient to account for all the 5-GHz flux observed by Goss & Shaver (1970). They suggested that an O5 star and little or no dust absorption of the continuum photons in the ionized region could fit the known parameters of RCW 38. Mizutani et al. (1987) present a Brγ map of the region (15- arcsec resolution), and find that Brγ emission largely follows the structure of the 10-μm images. From their observations they deduce an electron temperature of about 8000 K. They argue that IRS2 represents three O6 (ZAMS) stars rather than a single O5 star, although they do not preclude the possibility of an O5 star with a cluster of embedded stars.

Storey & Bailey (1982) present a NIR *K*-band image of the inner 2.5 arcmin of RCW 38. Their image shows a number of discrete sources surrounded by extended nebulosity. NIR photometry indicates that all the bright sources in the field are highly reddened point sources, and they infer visual extinctions of up to 60 mag. Allen & Meadows (1992) present a JHK' image of a larger region around IRS2. Their more sensitive observations show that the nebulosity is far more extended than indicated by the image of Storey & Bailey. The blue appearance of the nebulosity in the JHK' false-colour image hints that the extinction toward the nebulosity is not high.

Ligori et al. (1994) imaged a region $\sim 1.5 \times 1.5$ arcmin^2 at *JHK* centred on IRS2 with a spatial resolution of 0.89 arcsec pixel^{-1}. They resolve IRS2 into a cluster of at least five point sources within the central 16 arcsec, the beamsize used by FP74. The brightest source in this region dominates the observed flux and is saturated in their data. They also find a number of sources with large $H-K$ excess within their field of view, which may also be young embedded sources. One of their reddest sources is tentatively identified with FP74's IRS 3, detected at 10 μm. From their data Ligori et al. construct a *K*-band luminosity function, which they fit with a Miller–Scalo IMF to deduce a cluster age of ~ 2 Myr.

Due to the complex nature of this source, the large-beam *IRAS* observations at 12 and 25 μm of this region do not provide much insight, although Kuiper et al. (1987) are able to extract useful 60- and 100-μm fluxes, from which they deduce a cool dust temperature of 45 K and gas column density of 2×10^{20} cm^{-2}. However, from observations at 1 mm Cheung et al. (1980) derive a high column density of 8×10^{23} cm^{-2}, from which they infer a large visual extinction of 800 mag, indicating that RCW 38 lies at the front surface of a dense and massive (10^4 M$_\odot$) molecular cloud.

Detailed molecular observations of RCW 38 are rare. Gillespie, White & Watt (1979) mapped a region 1.0×0.5 deg^2 in the CO ($1 \rightarrow 0$) line with a 3.2-arcmin beam. They find that the CO is extended with a size of $\sim 20 \times 10$ arcmin^2, which corresponds to a linear size of 10×5 pc^2 at the adopted distance. The emission consists of two clumps connected by a bridge of material in an east–west direction. RCW 38E is associated with the H II region, while RCW 38W lies some 15 arcmin away. Observations with higher spectral resolution in the CO ($2 \rightarrow 1$) line by White & Phillips (1983) indicate that the CO emission suffers from large self-absorption in the direction of RCW 38E. More recently, Zinchenko, Mattila & Toriseva (1995) have mapped RCW 38E in CS ($2 \rightarrow 1$). Their data show the high-density gas ($> 10^4$ cm^{-3}) to be clumpy and not peaked at IRS1, but rather appears in a shell-like structure surrounding it. A large velocity gradient is evident, running from NE to SW through IRS1. The CS velocity agrees with the dip in the CO emission, confirming that the dip is due to self-absorption by foreground gas. Zinchenko et al. estimate that the region traced by CS has a mass of 1.5×10^3 M$_\odot$. Howe, Snell & Bergin (in preparation) have mapped RCW 38E in ^{13}CO ($2 \rightarrow 1$) and CS ($2 \rightarrow 1$). Their data show the gas to be very clumpy, with multiple velocity components along the line of sight. Their data also indicate that the region around IRS2 does not contain much dense gas, and appears as a hole in their CS integrated intensity maps.

As part of a programme aimed at studying the morphology and excitation of southern H II regions we have obtained both continuum and line mid-infrared (MIR) images, as well as a spectrum, of RCW 38. Observations of another H II region, G333.6–0.2, have already been published by Fujiyoshi et al. (1998). In the following section we describe our observations of RCW 38 using a newly commissioned MIR camera. In Section 3 we present our results and analysis of both the imaging and spectroscopic information, in terms of the excitation and density of the H II region, and the dust temperature. We discuss our results in Section 4, and finally present our conclusions in Section 5.

2 OBSERVATIONS

The imaging observations presented here were made with the Max-Planck-Institut für extraterrestrische Physik (MPE) MIR imaging system MANIAC (Mid And Near Infrared Array Camera) at the European Southern Observatory (ESO) 2.2-m telescope at La Silla in Chile. This instrument is based on a Rockwell 128×128 Si:As IBC array, with control and readout electronics provided by Wallace Electronics Inc. The instrument is designed to provide simultaneous imaging at both MIR and NIR wavelengths. So far, however, only the MIR channel has been completed in Phase I of the instrument construction project. The NIR channel (with a 256×256 InSb array) and an MIR Fabry–Perot etalon are to be added during Phase II, which is currently underway. More detail of the instrument construction and capabilities are provided by Böker et al. (1997). Work is currently in progress to improve the system efficiency and on-line data reduction procedures, as well as the major upgrades provided by the Phase II plan for this instrument. The Phase II upgrades to MANIAC are a joint undertaking between the MPE, UNSW, ADFA and Southern Cross University.

At the ESO 2.2-m telescope the instrument pixel size is 0.345 arcsec with a 44-arcsec clear field of view. Currently the instrument provides an *N*-band sensitivity of $1\sigma \simeq 2.5$ mJy arcsec^{-2} h^{-1} on the 2.2-m telescope. At this telescope we experienced quite large chopping offsets and structure in the image that could be removed only by beamswitching. The exact cause of this chopping structure was not determined, but we attribute it to the fact that the secondary on the 2.2-m telescope is barely undersized, and with the 60-arcsec or larger chops required with the field of view of MANIAC it is possible that we were chopping close to the edge of the primary mirror. Fortunately, the beamswitch reduced this structure to less than 1 per cent.

In MANIAC, each of the various filters appears not to be exactly parallel in the filter wheel, which introduces small spatial offsets (1–2 arcsec) when changing to different filters. The offset is quite stable, however, and is determined by comparing the position on the array of a standard star in the various filters. These offsets are included when image registration and overlaying are used.

The observations were made on the nights 1996 October 30 and 31 and November 1. Throughout these nights the visible seeing was between 0.3 and 0.65 arcsec, and well below the diffraction limit of 0.96 arcsec at 10 μm and 1.9 arcsec at 20 μm. The images of standard stars showed clearly diffraction-limited structure, i.e., Airy rings, at all wavelengths used.

In addition to the image data, we have spectroscopic observations

of RCW 38 between 8 and 13 μm, obtained using the UCL cooled grating spectrometer at the 3.9-m Anglo-Australian Telescope (AAT) on 1984 May 12. A description of the UCL spectrometer and observing procedures is presented by Aitken et al. (1985).

3 RESULTS AND ANALYSIS

3.1 Broad-band images

Fig. 1 shows the *N*-band (8–13 μm) and *Q*-band (17.3–22.7 μm) images. The images were centred on the position quoted for IRS1 by FP74, but the absolute pointing is uncertain. *N*-band images were obtained on all three nights, and Fig. 1 is the sum of these images. It represents 680 s of integration, including the chop and beamswitch overheads. The *Q*-band image was obtained on October 30 only, and represents a 480-s integration (including chop/nod). Both images were obtained using a 60 arcsec north–south chop/nod. Flux calibration was made with respect to η Sgr, which was taken to have a flux of 196 Jy at *N* and 73.3 Jy at *Q*. The original images significantly oversample the diffraction limit (0.345 arcsec pixel^{-1} and $\sim$ 1 and 2 arcsec diffraction FWHM at 10 and 20 μm), so the displayed images in Fig. 1 have been smoothed back to their respective diffraction limits with a Gaussian smoothing function.

Both the *N*- and *Q*-band images show similar extended emission in a ridge-like structure oriented approximately north–south, with fainter emission $\sim$ 20 arcsec west, and little emission immediately east of IRS1. The basic features of Epchtein & Turon's (1979) observations are evident, although we are able to identify at least one more position of local maximum of intensity in the southern part of the ridge at 10 μm, namely our source C. The ridge is a little more extended, or less peaked, at 20 μm than in the 10-μm image, although it is important to keep in mind the lower spatial resolution of the 20-μm image. The peak of IRS1 in both the *N*- and *Q*-band images coincides to less than the 10 μm diffraction limit. We have tentatively identified the compact peak of emission $\sim$ 15 arcsec east of IRS1 with the bright NIR source IRS2. FP74's map suggests a separation between IRS1 and IRS2 of $\lesssim$ 10 arcsec, but their spatial resolution was low and their positions are probably only good to $\pm$5 arcsec at best. There appears to be little or no emission from dust in the region immediately surrounding IRS2.

IRS2 itself appears to be slightly elongated in a roughly east–west direction. This is probably the result of two of the multiple components of IRS2 (as seen in the *K* band; e.g. Storey & Bailey 1982 and Ligori et al. 1994) which merge at the spatial resolution of these measurements. We do not, however, detect any of the other components of IRS2. Unfortunately, the NIR observations do not provide sufficient spatial information to allow us to register them with our images, and so a detailed comparison of the MIR and NIR morphology and spectral distribution is impossible. However, such a comparison is one of the design requirements for MANIAC, and will become possible after a further upgrade. We measure IRS2 to be around 2 Jy, which is consistent with emission from the photosphere plus free–free emission from an O5 star.

3.2 8–13 μm spectroscopy

The 8–13 μm spectrum is presented in Fig. 2. This spectrum amounts to 26 min of integration, chop/nod included, and was made in a 4.2-arcsec circular aperture. A 60-arcsec north–south chop/nod was employed. The observation is centred on the 10 μm emission peak, which corresponds to the source labelled IRS1 by FP74. Flux calibration and correction for telluric absorption features are made by reference to the standard star γ Cru with a flux at 10 μm of 4.5×10^{-15} W cm^{-2} μm^{-1}. The spectral resolution employed was $R = 40$, or 0.238 μm per resolving element.

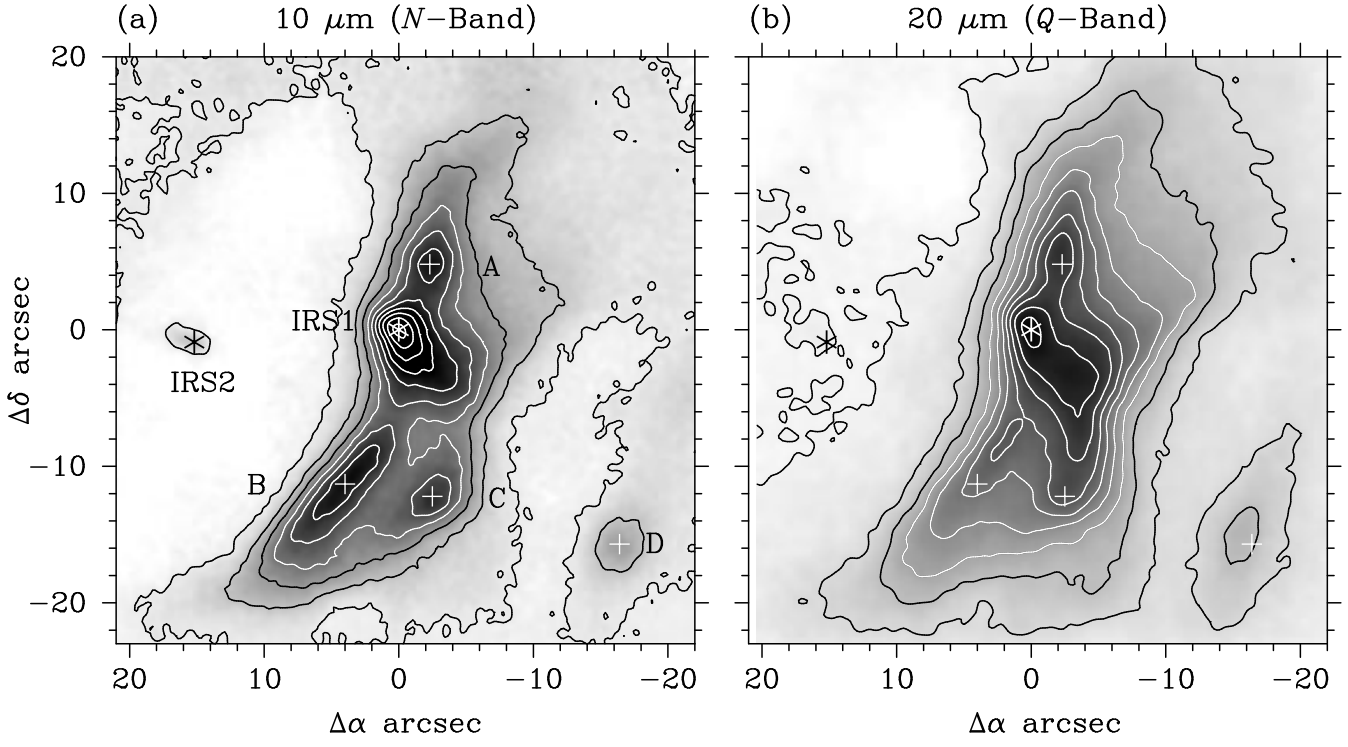

Figure 1. *N*- and *Q*-band images of RCW 38. Offsets are in arcsec from the peak of IRS1, which is labelled with an asterisk, as is IRS2 $\sim$ 15.5 arcsec E of IRS1. Also labelled A–D are four 10 μm emission peaks, which will be referred to in subsequent figures. Contours superimposed on the images are 5, 15, 25, ... 95 per cent of the peak of 1.44 Jy arcsec^{-2} (*N*-band) and 7.5 Jy arcsec^{-2} (*Q*-band).

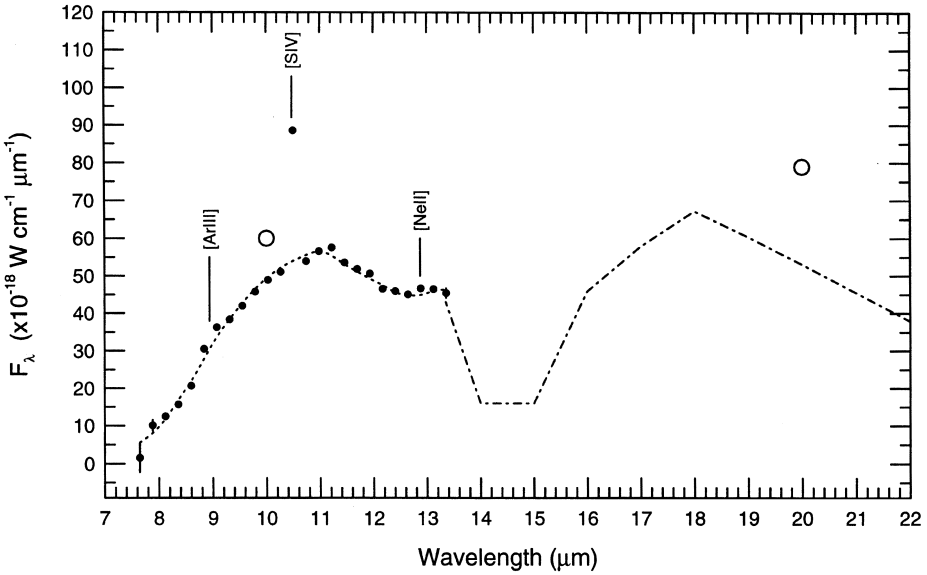

Figure 2. 8–13 μm spectrum of RCW 38 IRS1, obtained with the UCL spectrometer at the AAT. Filled circles show the observed spectroscopic data, and for all but a few points the error bars are smaller than the plotted point. The strong [S IV] emission feature is labelled (as are [Ar III] and [Ne II]), and the dashed line shows a fit to the continuum spectrum as discussed in Section 3.2. A further elevated point at 11.3 μm could possibly be the H9-7 line. The open circles show the *N*- and *Q*-band fluxes (from Fig. 1) determined for a 4.2 arcsec aperture centred on IRS1. Again the error bars are smaller than the plotted point. The dot-dashed line in the 13–22 μm region shows the extended fit using the dust temperature and absorptive optical depth determined from the 8–13 μm fit. The extended fitting is discussed in Section 3.4.

The spectroscopic observation of RCW 38 was made as part of a polarimetric study of this source, and as a result of the long integrations required, the S/N ratio for the spectroscopic data is excellent at around 250 per point. In Fig. 2 the error bars are only larger than the plotted point in a few cases at the very edge of the atmospheric window. The high S/N ratio allows for fairly tight constraints to be placed on some of the dust parameters. The polarimetric data will be presented in detail elsewhere, but these observations show polarized emission at about the 2–3 per cent level with a position angle of 138°, as well as some evidence for a small absorptive polarization component with a position angle of 75°. Accepting standard Davis–Greenstein-type grain alignment theory (Davis & Greenstein 1951), the polarimetry therefore indicates a magnetic field direction of between 48°and 75°, which is nearly normal to the elongated ridge in which IRS1 lies. Conversely, the interstellar magnetic field direction, determined from optical polarimetry of field stars, lies at 170° (e.g. Axon & Ellis 1976; Klare & Neckel 1979), almost orthogonal to the MIR magnetic field and closely parallel to the dust ridge. The implications of this will be explored in a forthcoming paper, together with imaging polarimetry observations.

The rising spectral energy distribution (SED) indicates emission from relatively cool dust, plus the notable feature of the strong [S IV] fine-structure emission line at 10.51 μm. We measure the [S IV] intensity as $8.2\pm0.5\times10^{-18}$ W cm^{-2} in a 4.2-arcsec aperture. On close examination of the spectrum the [Ar III] line at 8.99 μm is detected, though split over two detectors, with a line intensity of $(1.3\pm0.4)\times10^{-18}$ W cm^{-2} and the [Ne II] line at 12.81 μm is also weakly present with a line intensity of $(4\pm1)\times10^{-19}$ W cm^{-2}, both in a 4.2-arcsec aperture. These line strengths are observed values and have not been corrected for extinction.

3.2.1 Emission-line modelling

The presence of strong emission from [S IV] and only weak emission from [Ne II] and [Ar III] indicates a relatively strong ionizing radiation flux with an abundance of photons above the [S III] ionization potential of 34.83 eV (Genzel 1992). The ionization potential for [Ne II] is 40.96 eV and for [Ar III] it is 40.74 eV, and presumably most of the Ne and Ar has been ionized to the higher states, [Ne III] and [Ar IV] indicating a strong flux of photons with energies greater than 41 eV. On the other hand, the evident abundance of the [S IV] state (ionization potential = 47.3 eV), as indicated by the strong emission line, shows that photons with energies greater than 47.3 eV can not be so plentiful or these ions too would be ionized to the next higher state [S V]. Whilst we admittedly have no information on the abundances of the higher ionization levels, we feel that the combination of weak [Ne II] and [Ar III] emission but strong [S IV] emission serves to constrain the bulk of the ionizing photons to the range 40.7–47.3 eV.

To provide the required ionizing flux, we estimate that a star with effective temperature $T_{\rm eff}$ of at least 40 000 K is needed. This rough estimate is made by simply comparing our observed line ratios in RCW 38 to those observed by other authors in different H II regions, and for which a $T_{\rm eff}$ was inferred (e.g. Rank et al. 1978 for G333.6–0.2 and G298.2–0.3; Lester, Dinerstein & Rank 1979 for K3-50A; Lacy, Beck & Geballe 1982 for G298.2–0.3, RCW57 and G29.9–0.0; Simpson & Rubin 1984 for G45.1+0.1 and G29.9–0.0; Colgan et al. 1991 for G45.1+0.1 and K3-50A). Compared to all these sources, RCW 38 has the highest observed [S IV]/[Ar III] and [S IV]/[Ne II] ratios. This estimate is consistent with NIR (FP74) and FIR (Furniss et al. 1975) measurements which suggest a late O star or cluster of later type stars to be the exciting source. Similarly, the He I ($\lambda = 2.06$ μm)/Brγ ratio, which is often used as a constraint on massive star formation (e.g. Doyon, Puxley & Joseph 1992), is observed to be quite high in RCW 38 at 0.65 (Mizutani et al. 1987), which also suggests a minimum effective stellar temperature around 40 000 K. This method for determining stellar temperature, however, may not be very reliable for hot stars, as Shields (1993)

and Lumsden & Puxley (1996) find that the He I/Brγ ratio actually decreases rather than saturates at temperatures over 42 000K.

Even though we have limited information, with only two observed line ratios, in an attempt to confirm our arguments above and perhaps to investigate more fully the physics of RCW 38, we have used the CLOUDY photoionization code (version 90.03, Ferland 1993) to model our data. As input to the code we have used SEDs from photospheric LTE model atmospheres by Kurucz (1994) and non-LTE calculations by Pauldrach (private communication). This allows us to investigate the effect of the adopted stellar SED shape. Assuming that IRS2 represents the exciting star(s) of the H II region, from our images we were able to constrain the inner radius of the ionized region to be around 0.12 pc, which is in fact the separation between IRS1 and IRS2. Whilst this is a projection of the real separation on to the plane of the sky, given that we interpret the ridge as part of a region forming an elliptical shell around IRS2, we believe that the actual value is very close to this.

With little a priori information on elemental abundances we assumed that they were all solar. There is, however, some justification for this assumption. For instance, in a study of RCW 38 using far-infrared (FIR) transitions of [O III] in a $2 \times 2\,\mathrm{arcmin}^2$ beam Takami et al. (1987) infer an oxygen abundance very close to solar. Whilst this does not necessarily imply that this is also the case for Ar, S and Ne, we also note that RCW 38 has a similar galactocentric distance as the Sun, so that it should not be subject to the radial abundance gradients known to exist within the Galaxy (e.g. Simpson et al. 1995). Since our images clearly demonstrate the existence of dust in the ionized region we included dust in our models. The grains were of the Orion type as defined in Baldwin et al. (1991). The dust-to-gas ratio was such that 0.33 per cent of the mass is contained in graphites and 0.52 per cent in silicates (implying a gas-to-dust mass ratio of slightly more than 100). When comparing the model output to our observations we used extinction-corrected line ratios. The correction was performed using an A_V of 10 mag, a Draine & Lee (1984) extinction law, and a screen-type geometry. Finally, the nebular hydrogen density and stellar luminosity were treated as free parameters in the models, the former being assumed constant within any one model. This allows us to make independent determinations of the stellar type and gas density without any underlying assumptions.

Using the Kurucz SEDs we were able to fit both the extinction-corrected [S IV]/[Ar III] and [S IV]/[Ne II] ratios with an effective temperature, $T_{\rm eff}$, of about 46 000$\pm$2000 K and a density of $10^{4.0\pm0.2}$ cm^{-3}. The uncertainties indicate the ranges in each quantity observed when sampling the line ratios at either the inner or outer face of the model cloud. For instance, at the inner face a $T_{\rm eff}$ of around 44 000 K and a density of $10^{3.8}$ cm^{-3} are required, whereas at the outer face about 48 000 K and $10^{4.1}$ cm^{-3} are better. Lower density models, down to 10^2 cm^{-3}, and higher density models, up to $10^{5.5}$ cm^{-3}, provide progressively worse matches to the data. Our derived $T_{\rm eff}$ implies a single ZAMS star of spectral type between O5.5 and O4.5 as the ionizing source (Panagia 1973; Lang 1992; Hanson, Howarth & Conti 1997). Whilst we cannot exclude the possibility that a cluster of several lower $T_{\rm eff}$ stars could also provide a suitable match, the calculated ratios are very sensitive to the temperature and bolometric luminosity, and $T_{\rm eff}$ could be lowered by only about 1000 K for either face. The suggestion of Mizutani et al. (1987) of three O6 ZAMS stars ($T_{\rm eff} \sim 41\,000$ K) is not consistent with our data. Indeed, between about 10 and 100 such stars would be required to fit just one of the ratios. However, their suggestion of a single O5 star plus a cluster of embedded stars is clearly not ruled out. Additionally, in $L_{\rm bol}-T_{\rm eff}$ space the solutions for our observed line ratios begin to diverge beyond the locus of ZAMS stars, i.e., with higher $L_{\rm bol}$ and lower $T_{\rm eff}$, so that an ionizing star above the main sequence is also inconsistent with our data. In anticipation of our model in Section 4.2 for the heating of the dust in RCW 38, we also ran a dust-free model, and found results in agreement with those above.

If instead the Pauldrach SEDs are used the extinction-corrected line ratios can again be matched nicely, with the corresponding $T_{\rm eff}$ being in the range 45 000$\pm$2000 K and the density again $10^{4.0\pm0.2}$ cm^{-3}. Obviously the implied spectral type of the ionizing star is again between O4.5 and O5.5. In this case the solutions are not quite as sensitive to the temperature and bolometric luminosity, and at the inner face a model of three O6 ZAMS stars appears viable.

Unfortunately, there is little other published information on fine-structure line measurements of RCW 38 made in a similar beamsize to ours, with which we might further constrain densities (e.g., electron density using lines from the same element and ionization stage) and the exciting source and/or abundances (e.g., using lines from the same element but different ionization stages). From optical observations in a $17 \times 34\,\mathrm{arcsec}^2$ beam of [S II] and [O II] Danziger (1974) infers an electron density of 4×10^3 cm^{-3}, and Mizutani et al. (1987) derive 6×10^3 cm^{-3} from Brγ mapping, whilst Takami et al. (1987) infer an electron density of 10^4 cm^{-3} for their single-component model, and 5×10^4 cm^{-3} clumps embedded in 150 cm^{-3} ambient gas for their two-component model. Our derived spectral type of the ionizing star is similar to that inferred by other authors for RCW 38, as noted above and in our introduction.

It is worth noting the similar $T_{\rm eff}$ results obtained for the Kurucz and Pauldrach model SEDs. Given that the Kurucz SEDs are calculated in LTE, and that the Pauldrach SEDs include stellar winds and are non–LTE, the similarity is striking. The implication may be that the most important physics is already contained within the LTE models. Further testing on different sources, with a larger line set and where other parameters such as the nebular density and inner radius are already constrained, would be advantageous in determining whether observations of the type presented here can be used to test further developments in stellar atmosphere models.

To summarize, the best match between the model calculations and the observations, for both the Kurucz and Pauldrach SEDs, was for an inner radius of 0.12 pc, effective temperature of 43 000 to 48 000 K, and hydrogen density of around 10^4 cm^{-3}. Since we have set the inner radius of the model H II region to be the IRS1–IRS2 separation, and our spectral observations are centred on IRS1, we favour a $T_{\rm eff}$ at the low end of the quoted range, i.e., between 43 000 and 44 000 K, implying a spectral type of O5.5 V or O5 V.

3.2.2 *Continuum emission modelling*

Fitting the RCW 38 SED to an optically thick blackbody or optically thin silicate-like emissivity alone provides relatively poor fits to the spectrum ($\chi^2/n \simeq 50$). However, a simple two-component model fit with underlying optically thin silicate emission plus some silicate absorption by cold grains provides quite a good fit ($\chi^2/n \simeq 2.6$). The silicate dust emissivity function used in this case is derived from the deep absorption feature in W3 IRS 5 (Wright 1994). This emissivity function is similar to that for the Trapezium in Orion, but provides better fits to silicate emission/absorption from molecular cloud sources. The temperatures derived for the silicate dust from this fit are 175$\pm$6 K, which is suffering a modest 0.56$\pm$0.03 optical depth at 9.7 μm from cold silicate dust absorption. Assuming an extinction ratio $A_V/\tau_{9.7\mu\mathrm{m}} = 18.5$ (Roche

& Aitken 1984), we estimate the visual extinction towards IRS1 to be $A_V = 10.4$, which is in excellent agreement with the extinction of $A_V = 10.7$ over the extent of the H II region estimated by FP74. The resultant fit to the data is shown as a dashed line in Fig. 2.

3.3 [S IV] image

On 1996 November 1 we obtained an image of RCW 38 in the [S IV] 10.51-μm fine-structure line using a narrow-band filter centred on 10.51 μm (Δλ = 0.124 μm) with MANIAC. The continuum is subtracted from the emission line using the *N*-band continuum image scaled to the continuum level at 10.5 μm. The scaling information is obtained from the spectroscopic data of Fig. 2. Fluxes from corresponding 4.2-arcsec apertures on the [S IV] and *N*-band images are scaled to those of the spectra in the line and continuum at 10.5 μm. This continuum-subtraction technique relies upon the fact that the *N*-band image provides a reasonable representation of the 10.5-μm continuum, and that there are no extreme temperature or extinction variations across the image. The temperature map presented in Section 4.1 suggests that this assumption is reasonable, at least for the regions of sufficient S/N ratio to be of interest. Three images are presented in Fig. 3, the raw line plus continuum image, the *N*-band continuum used for subtraction and the continuum subtracted [S IV] image.

The [S IV] and dust thermal emission distributions are broadly similar, indicating that the gas and dust are well mixed in the ionized zone of RCW 38. However, there do seem to be some discrepancies where the continuum and fine-structure line emission do not match up exactly. The reason for these differences is not clear, and warrants further investigation with better continuum-subtraction techniques. We do note that the continuum peak D to the south-west corner does not show as a significant [S IV] peak, which is probably due to geometrical dilution and absorption of the photons capable of ionizing sulfur to the [S IV] state.

3.4 10/20 μm dust temperature map

From the spectroscopic data in Section 3.2 it is clear that the spectrum for RCW 38 shows evidence for emission and absorption from silicate-like dust grains. This means that to use the *N*- and *Q*-band images to produce a simple blackbody colour temperature map would produce misleading results. The presence of the silicate absorptive and emissive components needs to be accounted for before a useful dust temperature map can be produced. Unfortunately, we do not have any 20-μm spectroscopic data, nor is there any to be found in the literature or *IRAS* LRS catalogue.

We do not know the temperature of the absorptive material at 10 μm, but it is unlikely that this material would produce significant emission at 20 μm, so we have assumed that a proportional amount of absorption will occur at 20 μm. If we assume that the extinction is constant across the image, then it is still possible to extract a reasonable dust temperature from *N*- and *Q*-band images. Although we do not have any 10- or 20-μm spatially resolved spectroscopic data to confirm this assumption, the 2.2 μm images of Storey & Bailey (1982) and Allen & Meadows (1992) do not show any significant variations that might be attributed to variable extinction across the image. Additionally, FP74 infer a similar amount of extinction towards IRS2 ($A_V \simeq 12.8$) as we find towards IRS1 ($A_V \simeq 10.4$), indicating that the extinction in this region is relatively constant.

To derive the dust temperature across the image, we first need to determine if the simple two-component (single warm dust temperature) model is capable of being extended to the 20-μm region. If not, a second, cooler dust component may be needed, in which case it is impossible to extract any useful information from the limited amount of spectral information (i.e., two data points) in the two images. We have already assumed the extinction to be constant, and to make another assumption about a second, cool dust component would be stretching the data beyond credibility.

If we extend the two-component (single dust emission temperature) fit from Section 3.2 to longer wavelengths we obtain a prediction of the 20-μm flux that would result from a 4.2-arcsec aperture around IRS1. We can then compare the fluxes obtained from the *N*- and *Q*-band images with those of the model. We have extended the silicate emissivity function beyond 13 μm in 1 μm steps out to 24 μm. As we do not have observed spectroscopic data for W3 IRS5 in the 20-μm window, we have used emissivity data derived from the work of Scott & Duley (1996). These data are similar (though not identical) to other derived silicate emissivities (e.g. Draine & Lee 1984), but fortunately the shape of the silicate

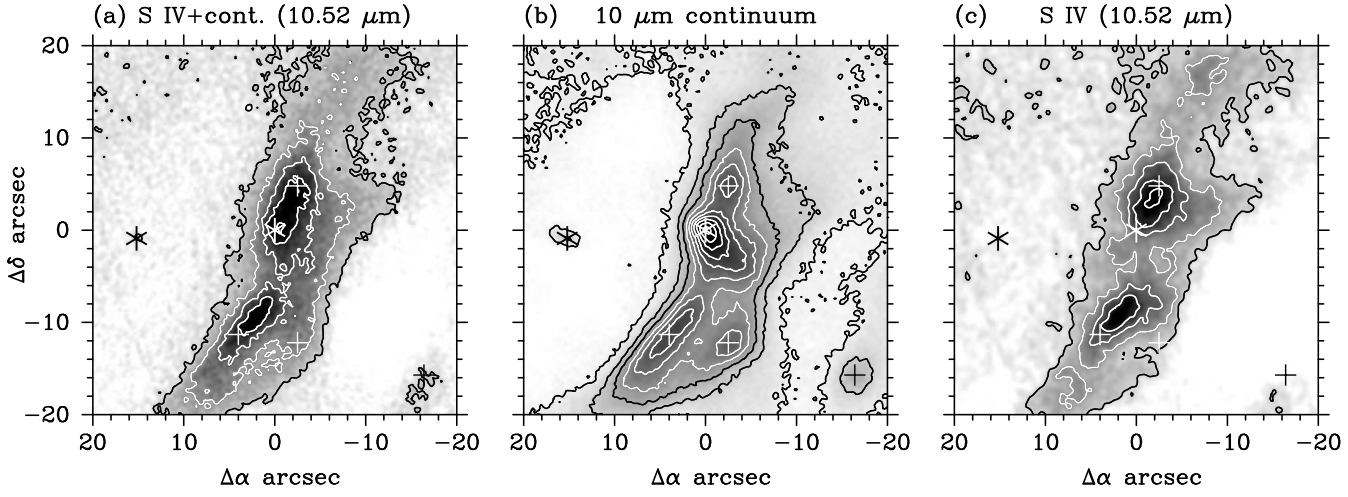

Figure 3. [S IV] image of RCW 38. From left to right the images are (a) the raw line plus continuum image (unsubtracted), (b) the *N*-band continuum used for subtraction, and (c) the continuum-subtracted [S IV] line image. Offsets are in arcsec from the peak of IRS1 in the *N*-band image. The positions of IRS1 and IRS2 are indicated with asterisks (cf. Fig. 1), and the features A–D (Fig. 1) are indicated with crosses. Contours superimposed on the images are 15, 35, ... 95 per cent of the peak of 1.09×10^{-18} W cm^{-2} arcsec^{-2} ([S IV] image) and 5, 15, ... 95 per cent of 1.44 Jy arcsec^{-2} (10 μm image).

resonance in the 20-μm region is not so acutely dependent on the grain parameters as the 10-μm region. This extended model fit is included in Fig. 2, and is shown by a dot-dashed line joining the 8–13 μm fit (short-dashed line) at 13.5 μm. The model is defined by the equation

$$F_\lambda = \Omega\, \epsilon_\lambda\, B(\lambda, T)\, \mathrm{e}^{(-\tau_{9.7\mu\mathrm{m}}\, \epsilon_\lambda)}, \quad (1)$$

where F_λ is the calculated flux, Ω is a parameter that normalizes the derived flux to the observed flux at 10 μm, ϵ_λ is the silicate emissivity function, $B(\lambda, T)$ is the Planck function at dust temperature T, and $\tau_{9.7\mu\mathrm{m}}$ is the absorption optical depth at the peak of the silicate resonance. This model is not different from earlier simple two-component fits (e.g. Aitken & Jones 1973; Gillett et al. 1975), but as it is to be used as the basis of the derived temperature map from the *N*- and *Q*-band images, it is restated explicitly here.

From this model we obtain 10- and 20-μm broad-band fluxes (i.e., integrating over the respective band) of 233×10^{-18} and 430×10^{-18} W cm^{-2} respectively. Equivalent fluxes extracted from a 4.2-arcsec aperture centred on IRS1 from the *N*- and *Q*-band images provide fluxes of around $(300 \pm 8) \times 10^{-18}$ and $(540 \pm 10) \times 10^{-18}$ W cm^{-2} respectively. Clearly, there is a calibration difference between the two data sets of about 25 per cent, but it is the ratio between the 10- and 20-μm data that is important in the determination of the temperature. The absolute calibration of disparate data sets is always difficult without very careful photometric monitoring throughout a night, and we would rarely claim absolute calibration better than this 25 per cent difference anyway. The ratio of model data $F_{20\mu\mathrm{m}}/F_{10\mu\mathrm{m}}$ is 1.85, and from the broad-band images it is about 1.8, which provides remarkably good agreement. We believe that this validates the simple two-component model for use in the 20-μm window in this particular source.

Using a modified colour temperature (as described above) that takes account of the presence of silicate grains, we can derive a dust temperature for each common point in the *N*- and *Q*-band images, and Fig. 4 shows the dust temperature map derived in this way. To ensure that the different spatial resolution in the *N*- and *Q*-band images does not produce spurious features, the *N*-band image was smoothed to the *Q*-band diffraction limit before the colour temperature map was constructed. It should be remembered, too, that we have made the assumption that the silicate extinction is the same over the whole image, and that the chemical composition of the dust also remains more or less constant. For these reasons, plus the fact that a distribution of grain sizes might be expected, each of which perhaps attains a different equilibrium temperature, our temperature image is most useful for determining spatial trends in the dust temperature, rather than absolute values.

From Fig. 4 we see that the temperature is highest in the centre of the ridge-like emitting region, and drops off rapidly to both the east and west. We do not attribute any significance to the high temperatures to the far north or far west of the map (except for source D at $\Delta\alpha \simeq -18''$, $\Delta\delta \simeq -16''$), as the S/N ratio in these regions of the *N*- and *Q*-band images is not sufficient to determine reliable temperatures.

In the region around IRS1 there is a reasonable temperature peak, with the peak contour of 170 K. There is also a slightly stronger dust temperature peak some 15 arcsec to the south-east of IRS1. This temperature peak corresponds to the intensity of peak B in the *N*-band image. Although it is only about 60 per cent as bright as IRS1, the temperature here is about 175–180 K compared with

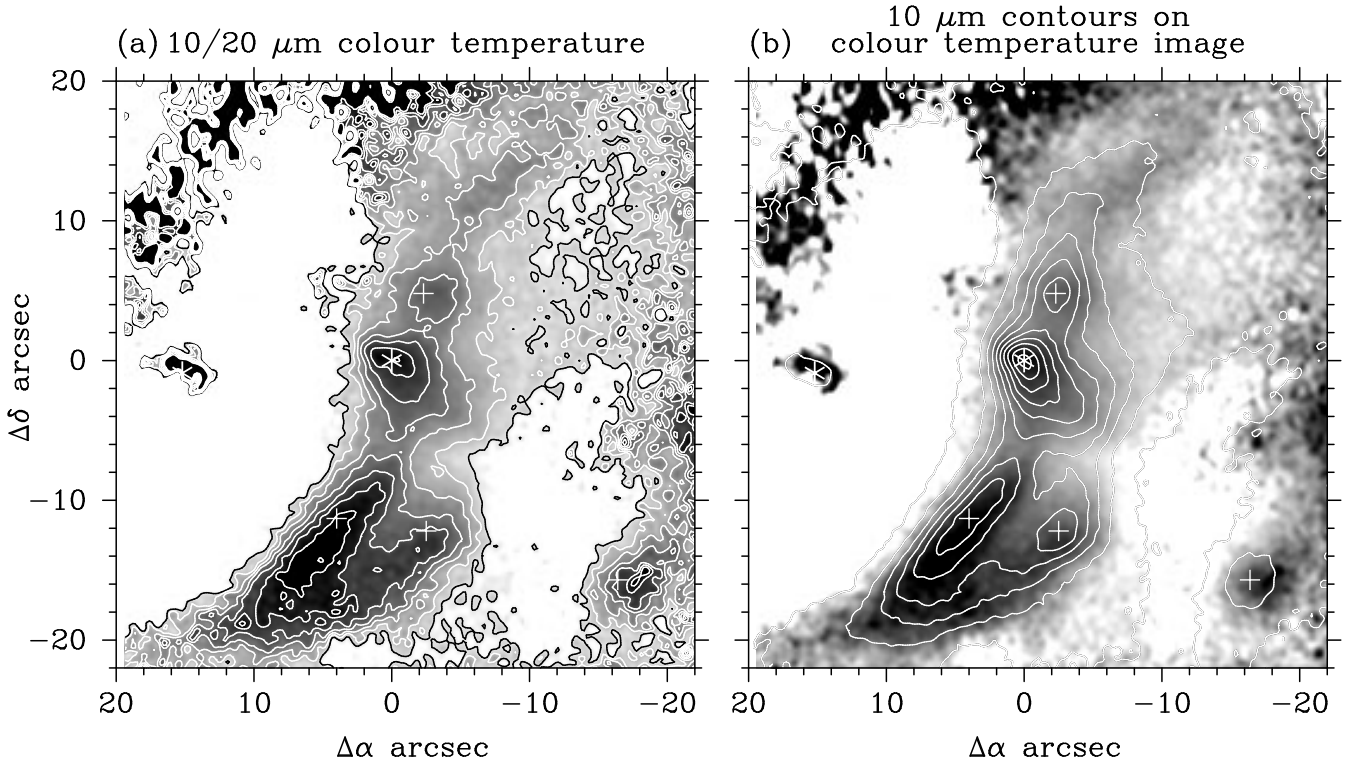

Figure 4. 10/20 μm colour temperature image of RCW 38. Offsets are in arcsec from the peak of IRS1 in the *N*-band image. In (a) we present the colour temperature image, while in (b) we present the same image with the 10-μm contours overlaid. The positions of IRS1 and IRS2 are indicated with asterisks (cf. Fig. 1), and the features A–D (Fig. 1) are indicated with crosses. The contour around the position of IRS1 is 170 K, and contours decrease in 5-K increments to the bottom contour of 145 K (shown in black). The maximum temperature contour around the peak to the south-east of IRS1 is 175 K. The 10 μm contour levels are the same as those in Fig. 1.

170–175 K at IRS1. IRS2 appears as a hot source (> 200 K) about 15 arcsec east of IRS1.

3.5 Dust opacity and mass

Having determined the dust temperature in the previous section, it is now possible to calculate the emissive opacity and mass of the dust. Before doing so, however, it is prudent to recognize the limitations of this calculation. In particular, we assume that the previously calculated temperature represents a single and uniform grain temperature along the whole line of sight. Panagia (1975) and Natta & Panagia (1976) have presented criticisms of this assumption, which they say leads to an underestimate of the dust mass. As noted above, a distribution of temperatures might be expected on the basis of a distribution of grain sizes and/or compositions. Therefore, once again our opacity image is most useful in showing spatial trends. Nevertheless, with the above approximation in mind, we can at least obtain an estimate of the dust opacity, and hence also the dust mass. Using the temperature distribution as determined previously and the observed flux from the *N*-band image, we have determined the opacity distribution by using the following equation:

$$\tau_{\mathrm{em},N} = F_N / B(N, T), \tag{2}$$

where $\tau_{\mathrm{em},N}$ is the emissive opacity in the *N*-band, F_N is the observed *N*-band flux, and $B(N, T)$ is the blackbody flux at the derived colour temperature.

In Section 3.2.2 we noted that the spectrum of IRS1 shows an absorptive optical depth of $\tau_{9.7\mu\mathrm{m}} = 0.56$, which is attributed to a layer of cold silicate grains in front of the RCW 38 region. The 9.7 μm optical depth represents the peak of the absorption but, using the same silicate emissivity function as Section 3.2.2, we find that the average emissivity over the *N* band is 0.61 of the peak 9.7-μm emissivity (i.e., $\tau_{N\text{-band}} = 0.61\tau_{9.7\mu\mathrm{m}}$). So, to account for the absorbing material, we deredden the *N*-band fluxes by $\mathrm{e}^{0.34}$. Given this correction, the opacity distribution is presented in Fig. 5.

First, it should be pointed out that the chain of high-opacity points around the inner rim of the IRS1 ridge are undoubtedly an artefact caused by poorly determined temperatures in these regions of low S/N ratio. Also, the opacity image has been smoothed using a Gaussian smooth function with FWHM = 3 pixels. In the regions where the S/N ratio in the original data is high, and where the dust temperatures are well determined (i.e., in the ridge) the opacities are reasonably determined. We see in the opacity map that IRS1 does not appear as a significant peak, implying that this region is not simply a dust density enhancement. In fact, the higher opacities occur on the outer edge of the ridge, i.e., away from IRS2. Apparently the bulk of the material is concentrated in the region away from the area of the most intense emission.

Given the opacities, it is also possible to determine a total dust mass. To achieve this, we assume that all the grains are silicate, and use the silicate dust mass absorption coefficient ($\kappa = 3000\ \mathrm{cm^2\ g^{-1}}$ at 9.7 μm) from Draine & Lee (1984) and the distance (d) to the source of 1.7 kpc. We then determine a dust mass for each pixel by using the following equation:

$$M_{\mathrm{dust}} = \tau_{\mathrm{em},N}\, d^2 / \kappa. \tag{3}$$

Integrating over the ridge, an area of 350 arcsec^2, we obtain a total dust mass in the ridge of around $5.7 \times 10^{-4}\ \mathrm{M_\odot}$. If we take a normal gas-to-dust ratio value of around 100:1, we find a total mass in the

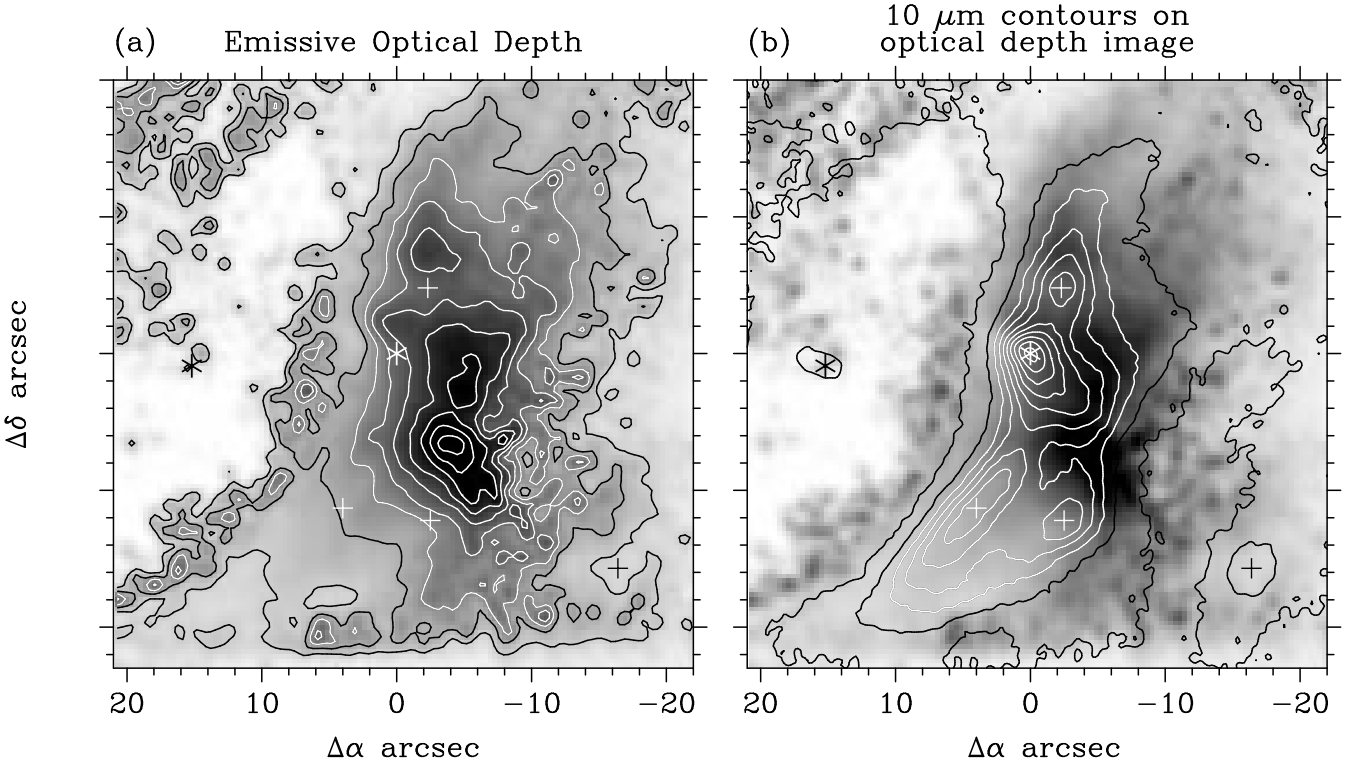

Figure 5. The emissive opacity distribution for RCW 38. Offsets are in arcsec from the peak of IRS1 in the *N*-band image. In (a) we present the emissive opacity image, while in (b) we present the same image with the 10 μm contours overlaid. The positions of IRS1 and IRS2 are indicated with asterisks (cf. Fig. 1), and the features A–D (Fig. 1) are indicated with crosses. The contours are 5, 15, ... 95 per cent of the peak of 0.038 in the opacity image, and 1.44 Jy arcsec^{-2} in the *N*-band image. It is interesting to note that the peak in opacity occurs on the outer edge of the ridge of emission, whereas the peaks in temperature and flux lie nearer the inner edge.

ridge of around 0.057 $M_\odot$ of gas and dust. However, as noted in Section 4.2, dust may be depleted in the region surrounding IRS2, and so this mass estimate may represent a lower limit to the true mass of the ridge.

4 DISCUSSION

4.1 A wind-blown cavity around IRS2

The region around IRS2 contains very little thermal emission, and almost no [S IV] emission, despite the proximity of the ionizing source, indicating that this space is basically clear of dust and gas. From the 2.2 μm images we know that IRS2 is a hot source located to the east of IRS1. We propose that IRS2 is the powering source for the region, and that the region around IRS2 represents a cavity blown out by the stellar wind of the young, hot star (or stars) inside IRS2. The ridge of emission around IRS1 shows the edge of the cleared cavity, which has a higher density of material, and in fact represents the outer shell.

At the distance of RCW 38, the 15 arcsec between IRS1 and IRS2 represents only 0.12 pc (projected on the sky). Now the terminal wind velocity of an O5 star is around 3000 km s^{-1} (e.g. Lamers, Snow & Lindholme 1995), and so a completely clear cavity between IRS1 and IRS2 could be crossed in just 39 yr by the wind. The normal mass-loss rate for this type of star is around 1×10^{-6} $M_\odot$ yr^{-1} and could contribute at best a few per cent of the observed mass in the ridge in the evolutionary time-scales of this region. Most likely, the ridge material around IRS1 results from pre-existing dust and gas from the H II region being swept up by the wind into a shell.

If we assume an initial cloud density of 10^4 cm^{-3} (as implied by our emission line modelling), plus a mass-loss rate and wind velocity as above, then by simple momentum transfer from the wind to the swept-up region, we calculate a period of around 1.5×10^4 yr to sweep out the cavity to the outer radius of IRS1. At this point the outward velocity of the shell is about 6 km s^{-1}, and if the wind sweeps all material into the shell, then the shell itself will have a mass of about 7.8 $M_\odot$ by the time it reaches the radius of IRS1. If we assume the IRS1 ridge covers about a quarter of the total shell surrounding IRS2, then we would expect about 2 $M_\odot$ in the IRS1 ridge. This mass estimate is consistent with that determined from the opacities earlier. We will revisit the mass of the RCW 38 ridge in Section 4.2.4. We do note, however, that our picture for the cavity clearing process is different to that traditionally inferred for the expansion of dusty H II regions, namely the high pressure of the ionized gas and radiation pressure on dust grains (e.g. Mathews 1969).

It is interesting at this stage to compare our data with models of expanding H II regions. The molecular observations mentioned in our introduction presented a picture of high-density gas (> 10^4 cm^{-3}) surrounding the region imaged by ourselves, which itself does not contain much dense gas. This is typical for the expansion of a Strömgren ionization front, and is similar to the models of Bodenheimer, Tenorio-Tagle & Yorke (1979) where ionization and shock fronts produced by a massive new-born star propagate into the ambient molecular cloud.

On the other hand, we may be seeing only the inner zone of a much more extended region. FP74 found 10 μm emission extended over a much larger region than we have imaged, as did Mizutani et al. in the Brackett γ line of hydrogen, and both our *N*- and *Q*-band images show what could be a second cavity and ridge (source D) about 10–15 arcsec west of the IRS1 ridge. Perhaps the shell creation is an episodic event, with incomplete clearing of the cavity with each event.

Finally, we note that the cavity is not spherical around IRS2, but rather elliptical. For instance, note the emission in the north-east corner of our *N*-band image. It may be that the presumed outflow finds it easier to expand toward the north-west and south-east of IRS2 due to lower density material along these directions. On the other hand, magnetic fields may also influence the shape of the cavity. For instance, the major axis of the ellipse is closely aligned with the interstellar magnetic field, yet almost orthogonal to the field determined from our spectropolarimetric observations mentioned in Section 3.2.

4.2 Heating of the dust in the IRS1 ridge

A remarkable feature of our colour temperature image in Fig. 4 is the relative constancy of the temperature over a large area. The variation is only ±15 K from the 'average' of 160 K. There is a hint that this constancy extends over an even larger area in the work of FP74. Whilst FP74 do not present a colour temperature map, they do state that the [10 μm] – [20 μm] colour does not change by more than 0.3 mag over the face of RCW 38. What mechanism can produce such a constant temperature, even though regions of the source are at significantly different projected separations from the presumed exciting star IRS2?

4.2.1 Direct heating of dust

Direct heating of the dust by IRS2 is undoubtedly occurring at some level. We investigate the contribution of this heating source by using a radiation transfer model to determine what dust temperature one would expect from direct heating of a dust shell at the distance of IRS1 (0.12 pc) away from a central hot source (IRS2).

The model used is based on the quasi-diffusion method, in spherical geometry, of Leung (1975, 1976), as implemented by Mitchell & Robinson (1978, 1980). While spherical symmetry may not be entirely appropriate to RCW 38, given the optically thin nature of the dust distribution and the fact that the model of Leung solves the radiative transfer problem in spherical symmetry without significant approximation, the results obtained for the dust temperature are likely to be reasonable.

In the model we have assumed that the illuminating source is IRS2, of spectral type O5.5V, with $T_{\rm eff} = 44\,000$ K and luminosity $L = 6 \times 10^5$ $L_\odot$. The inner and outer boundaries of the dust shell were assumed to be located at 0.09 and 0.214 pc from IRS2 respectively, and the dust density distribution has been assumed to follow a power law, $\rho = \rho_0 r^n$, where the index n was treated as a free parameter. However, since the shell is not very extended, ($R_{\rm max}/R_{\rm min} \sim 2.4$), the value of n is not critical. The optical depth has been varied from optically thin to optically thick ($\tau_{10\mu{\rm m}} = 0.001$ to 20) to investigate the opacity's effect on the dust temperature and temperature distribution. While an optical depth of around 0.5 was previously determined for IRS1, this is a different line of sight from that which a photon from IRS2 sees, and so the wide range of opacities is required to fully investigate the parameter space. Models with a single grain species have been used, with the grain species being pure astronomical silicates and astronomical silicates coated with a water ice mantle (see Robinson, Smith & Hyland 1992 for more details of the assumed opacity law for these grains). Carbon-based grains were not used in this instance, as the spectrum from Section 3.2.2 shows no evidence for a significant contribution

Table 1. Grain temperature as a function of radial distance from IRS2.

Grain radius	T(K)		
(μm)	$r = 0.09$ pc	$r = 0.15$ pc	$r = 0.21$ pc
0.01	224	108	83
0.02	206	116	87
0.05	168	126	102
0.10	142	118	101
0.10, 0.20[1]	141	100	77
0.20	122	105	92
0.50	100	89	79
1.00	87	78	69
2.00	74	67	59

[1]Core–mantle grain with silicate core of radius 0.10 μm and water ice mantle of radius 0.20 μm.

form anything other than silicate based grains. The grain radius has been varied within the range $a = 0.01 - 2.0$ μm.

The temperature of pure astronomical silicate grains as a function of radial distance for various grain sizes is shown in Table 1 for the case $n = -2$ and $\tau_{10\mu m} = 0.05$. It may be seen that as the grain size increases the temperature at the inner boundary of the dust shell decreases significantly, as expected. In general, the presence of a pure water ice mantle makes little difference to the grain temperature at the inner boundary of the shell, but reduces it somewhat within the shell itself, and of course it will affect the SED significantly.

From these results we derive two important points. First, the population of small grains, which dominate the number density, are too hot at the inner edge of the shell compared with the temperatures observed and, secondly, direct heating of the dust predicts a significant temperature gradient (on the order of 50 K) from the inner to outer edges of the dust shell. In the temperature map (Fig. 4) there is very little evidence for such a temperature gradient. The temperature is seen to be remarkably uniform (though with some small variations), given that parts of the dust ridge are further from IRS2 by at least a factor of 2 than the inner edge of the shell. So, whilst direct stellar radiation contributes to the dust heating, it definitely cannot dominate it.

4.2.2 Dust heating due to trapped Lyα photons

The Strömgren radius for a pure hydrogen nebula surrounding an O5.5 star is only about 0.2 pc if the nebula density is on the order of 10^4 cm^{-3} (and neglecting an inner cavity). This means that most of the $\sim 10^{49}$ Lyα-producing photons per second from IRS2 are resonantly trapped within this volume, and ultimately are absorbed by dust grains. This can lead to a powerful heating mechanism for the dust in the IRS1 ridge, which lies within the Lyα trapping zone. Indeed, a hint that this may in fact be the case is provided by FP74. They find that the 1–25 μm luminosity is comparable to that of the Lyα photons that are resonantly trapped within the ionized volume. Additionally, the inferred luminosity of IRS2 is consistent with that expected from a main-sequence star whose ultraviolet output beyond the Lyman limit is not significantly different from that required to supply the observed radio flux, implying that the dust does not compete effectively with the gas for the primary ionizing photons. Indeed, in our photoionization models of Section 3.2.1 we find that, with a normal gas-to-dust ratio of 100, about 40 per cent of the Lyman continuum photons are absorbed by dust, which is inconsistent with the inferred Lyman continuum and observed radio fluxes being equal. However, with a gas-to-dust ratio of 10^4 or higher, there is essentially no effective absorption of Lyman continuum photons by dust. FP74 infer that absorption by trapped Lyα photons is the primary heating mechanism of the dust. We then use this as a working hypothesis, and examine under what physical conditions the dust can be heated to the temperatures we observe.

We can estimate the heating effect of the Lyα photons if we equate the heating rate due to the Lyα photons, $G_{L\alpha}$, with the cooling rate of the dust, $L_r(T_d)$, and then solve for the dust temperature, T_d. We assume here that the energy radiated by the grain is essentially the same as that in thermodynamic equilibrium at temperature T_d. Following the treatment of Spitzer (1978), we find that the dust heating due to Lyα photons is given by

$$G_{L\alpha} = Q_{L\alpha} F_{L\alpha} E_{L\alpha}, \tag{4}$$

where $Q_{L\alpha}$ is the dust grain efficiency factor for absorption of Lyα photons, $F_{L\alpha}$ is the flux of Lyα photons crossing the surface of a grain per unit projected area per second, and $E_{L\alpha}$ is the energy of the Lyα photon. The Lyα flux is given by

$$F_{L\alpha} = \frac{z_{L\alpha} n_e n_p \alpha^{(2)}}{\sigma_d n_d Q_{L\alpha}}, \tag{5}$$

where $z_{L\alpha}$ is the fraction of recombinations in levels $n \geq 2$ that lead to emission of a Lyα photon (which we take to be 0.68 as given by Spitzer, but it could be higher at the density of RCW 38), n_e and n_p are the electron and proton number densities respectively, $\alpha^{(2)}$ is the recombination coefficient (here equal to 3.1×10^{-13} cm^3 s^{-1}, again from Spitzer), σ_d is the dust grain geometrical cross-section (i.e., πa^2), and n_d is the dust grain number density. We will assume that $n_e = n_p = n_H$. This then leads to an expression for the heating rate:

$$G_{L\alpha} = \frac{z_{L\alpha} n_H^2 \alpha^{(2)} E_{L\alpha}}{\sigma_d n_d}. \tag{6}$$

Our modelling of the radiation field in RCW 38 has previously indicated a gas density of around $n_H \simeq 10^4$ cm^{-3}, so it remains to determine the dust cross-section and number density in order to evaluate $G_{L\alpha}$.

We assume that the grains are all spherical and of the same size, say 0.1 μm in radius. We can therefore find the volume of a grain and, using the density of silicates as 3 g cm^{-3}, also the mass of a single grain. Assuming that the gas is composed mostly of hydrogen, with 10 per cent by number of helium, we can then write

$$R\, m_d\, n_d \;=\; 1.4\, m_H\, n_H, \tag{7}$$

where R is the gas-to-dust mass ratio, and m_d and m_H are the mass of a dust grain and a hydrogen atom respectively. Therefore the Lyα heating rate can be expressed as

$$G_{L\alpha} = \frac{z_{L\alpha} \alpha^{(2)} E_{L\alpha} m_d}{1.4 \sigma_d m_H} R\, n_H. \tag{8}$$

To determine the equilibrium dust temperature, we equate the heating rate to the cooling rate, L_r, which can be expressed in the following equation:

$$L_r = 4\pi \iint Q_{abs}(a, \lambda) B(\lambda, T)\, d\lambda\, da, \tag{9}$$

where $Q_{abs}(a, \lambda)$ is the absorption efficiency factor for grains of radius a at wavelength λ. To solve this expression for the temperature T_d, we again assume that the grains are single-sized, and that the efficiency factor is a constant and can be represented by a mean value in the MIR spectral region. This then leads to the simpler equation

$$L_r = 4\pi \sigma_{SB} T_d^4 < Q_{MIR} >, \tag{10}$$

where σ_{SB} is the Stefan–Boltzmann constant. Equating $G_{L\alpha}$ and L_r, we find

$$T_d^4 = \frac{z_{L\alpha}\alpha^{(2)}E_{L\alpha}m_d}{5.6\pi\sigma_{SB}\sigma_d m_H < Q_{MIR} >} R\, n_H \quad (11)$$

We take $< Q_{MIR} >$ here to be 0.04. This represents the mean of the efficiency factor from $\sim$ 6–25 μm, which we derived from the optical constants of various types of amorphous silicates (e.g., those of forsterite in Scott & Duley 1996, a pyroxene of approximate cosmic abundances in Jäger et al. 1994, glassy bronzite in Dorschner et al. 1988, astronomical silicate in Draine & Lee 1984, dunite in Penman 1976, and olivine and enstatite in Day 1979). Then, substituting in the relevant numbers, i.e., $n_H = 10^4$ cm^{-3} for IRS1, we find that with $R = 100$ the expected dust temperature is only of the order of 40 K. In order to reach the temperatures we observe, namely $\sim$ 175 K at IRS1, the gas-to-dust mass ratio must be 4.55×10^4 for $n_H = 10^4$ cm^{-3}.

We note that this is not affected by using a different grain size. As long as the Rayleigh approximation (i.e., $2\pi a \ll \lambda$) is valid, the decreased/increased heating rate for a smaller/larger grain is offset by a similar change in the efficiency factor. However, if a grain size distribution is used, it is probable that each size will attain a different temperature. Additionally, the gas-to-dust ratio is affected if a different grain composition is used, such as graphite; this has been suggested by Tielens & de Jong (1979) to be an important contributor to the 5–15 μm continuum emission of H II regions. Graphite will attain a higher temperature because of its lower efficiency factor in the MIR than silicates, by about a factor of 3–4 (e.g. Draine & Lee 1984). In that case a gas-to-dust mass ratio of $\geq 10^4$ can produce the same temperature for IRS1 as given above. Also, if the silicates have a mantle of organic refractory material, as is postulated by Li & Greenberg (1997), the grains will be hotter for a given value of R. For example, with a mantle whose volume is the same as the silicate core, $< Q_{MIR} >$ is reduced by about a factor of about 2, and so $R \simeq 2.0\times10^4$ cm^{-3} is required to reach 175 K. Nevertheless, the bottom line is that if resonant Lyα absorption is the dominant heating source for the dust, a dust depletion of at least several 100 from the standard ISM gas-to-dust mass ratio of 100 is required within the RCW 38 ionized zone.

Such a large dust depletion has previously been inferred for the ionized zones of H II regions, and was the subject of much debate in the literature in the 1970s. For example, in his models of dusty H II regions Wright (1973) found that the dust had to be depleted by factors of order 1000 over the ISM value in order that Lyα photons dominate the heating, *and* that a constant temperature be produced in the ionized zone. In his undepleted model a temperature gradient exists with increasing distance from the central star, which we *do not* see. Panagia (1975) and Natta & Panagia (1976) criticized observational findings of dust depletion on the basis that in some instances a direct comparison of the dust mass from MIR observations and gas mass from radio observations was used. They found that the common assumption of a single dust temperature leads to an underestimate of the dust mass, and when a more realistic temperature distribution is used a significant depletion is no longer found, if any at all.

Whilst this may be true, we note that our conclusions for RCW 38 are independent of the dust mass we derive. Rather they depend only on the relative invariance of the temperature throughout the RCW 38 ridge, a direct prediction of Lyα models. Indeed, even the value of the temperature itself is of only secondary importance. Tielens & de Jong (1979) reconciled the differences in the literature and, on the basis of a very detailed model of the spectral energy distribution of the W3A IRS1 H II region, presented strong arguments for large dust depletions inside H II regions. They also proposed several mechanisms whereby the dust may be depleted, such as by radiation pressure from the central star or by sputtering by energetic particles. Hackwell et al. (1978) came to a similar conclusion of significant dust depletion for W3 IRS1, as did Aitken, Griffiths & Jones (1977) for G333.6–0.2, on the basis of MIR emission and colour temperature maps, which are similar in nature to our images of RCW 38. More recently, detailed models (e.g. Chini, Kreugal & Kreysa 1986; Hoare, Roche & Glencross 1991) have also shown evidence for dust depletion in H II regions.

4.2.3 *Application of Lyα heating*

Having concluded that the dominant dust heating mechanism may be absorption of resonantly trapped Lyα photons, it remains to determine what might cause the slight, yet still apparent, temperature variations within the RCW 38 ridge, for example, amongst the different clumps A–D. Looking at equation (11) again, it can be seen that by changing either the gas-to-dust mass ratio R, whilst keeping the hydrogen density n_H constant, or changing n_H whilst keeping R constant, slight temperature variations can easily be produced. Of course, changing both can also provide a similar result. Therefore, variations in these quantities could be responsible for the slight temperature changes observed throughout the ridge. This was also suggested by Wright (1973). However, we can go even further than this and use the Lyα model to predict values for n_H and R for all the clumps, using equations (6) and (10), together with the following equation:

$$dF_\lambda = \frac{\kappa m_d dV}{d^2} n_d B(\lambda, T), \quad (12)$$

where dF_λ is the flux observed at wavelength λ from a volume element dV, and all other quantities have previously been introduced. This is just a simple rearrangement of equations (2) and (3), where $\kappa = 3Q_{abs}/4a\rho$, ρ is the density of silicates, and $M_{dust} = n_d m_d dV$.

The previous equations tells us that when comparing the fluxes of the different clumps within RCW 38, the only important parameters are the dust number density and temperature of the clump. All other parameters can be assumed to be the same. Therefore, if we use IRS1 as a standard, for which we know the flux, dust density and temperature, we can express the flux of a particular clump, for which we only know its flux and temperature, as a fraction of the flux of IRS1, and thereby derive the number density of the dust for each clump. Since we know the temperature of the clump, we can use equation (10) to derive the heating rate (assuming that it is equal to the cooling rate), and then use equation (6) to solve for n_H, the gas density. Doing so yields the values of n_d, $G_{L\alpha}$, n_H and R for clumps A–D in Table 2. It is noteworthy that the Lyα heating model is able to account for the difference in both fluxes *and* temperatures between all the clumps within the ridge, e.g., IRS1 and source B, for which the temperatures are the same yet the fluxes differ by a factor of 2.

We can perform a similar calculation for the eastern and western rims of the ridge. Note that at the eastern rim the observed temperature is lower than in the middle of the ridge, despite the fact that it is closer to IRS2. Perhaps here, nearest the cavity, the gas density is lower and/or the gas-to-dust mass ratio higher than in the middle due to the proximity to IRS2 and its wind. Indeed, this is shown to be the case in Table 2. With regard to the western rim, since its temperature is similar to that of the eastern rim it may be

Table 2. Gas densities and gas-to-dust mass ratios within the RCW 38 ridge.

Source	Flux *N*-band	T_d K	n_d $\times10^{-11}$	$G_{L\alpha}$ $\times10^3$	n_H $\times10^3$	R $\times10^4$
IRS1	1.00	175	4.10	26.8	10.00	4.55
A	0.55	160	4.58	18.7	8.83	3.60
B	0.55	175	2.25	26.8	7.42	6.14
C	0.45	160	3.74	18.7	7.88	3.98
D	0.15	165	0.97	21.1	4.33	8.29
E&W	0.10	145	1.94	12.6	4.72	4.54
NSP	0.50	155	5.40	16.5	9.00	3.10
SSP	0.50	165	3.25	21.1	7.91	4.54

Notes: The *N*-band fluxes have been expressed relative to that at IRS1. The dust and gas number densities are expressed in terms of cm^{-3}, whilst $G_{L\alpha}$ is in units of erg s^{-1} cm^{-2}. For all sources the ratio of the *Q*-band flux to that at IRS1 is also consistent with the values quoted. E and W refer to the eastern and western rims of the ridge respectively, whilst NSP and SSP refer to the northern and southern [S IV] peaks respectively.

thought that its properties would be similar to those in the east. That may be true, perhaps strengthening the case for a second cavity between the ridge and source D, but we must also be careful here. This is the region where our opacity image peaks, indicating perhaps an enhancement in the dust grain column density. As noted by Martin (1978), if there are too many grains the diffuse Lyman α flux does not build up and the grain temperatures are depressed.

Although all of our above treatment has made some fairly simplifying assumptions, e.g., a single grain size and a single dust temperature, we believe that it is the most direct and transparent way of presenting the effects of Lyα heating. Additionally, we do not know what type of size distribution might exist within the ionized zones of H II regions, such as its form and the maximum and minimum sizes. It might be expected that the harshness of the environment there, in terms of both the particle and photon radiation as well as mechanical motions, would change these parameters from their interstellar counterparts as given by Mathis, Rumpl & Nordsieck (1977). We should reiterate, however, that the numbers we present here for the dust temperature, and hence n_d, n_H and R, are somewhat uncertain. For instance, if the hydrogen density at IRS1 were to be lower by a factor X, then all other H densities would also decrease by X, R would increase by X, and n_d would decrease by X^2.

4.2.4 Ridge mass revisited

In this paper we have used two methods to estimate the mass of material comprising the RCW 38 ridge. It is interesting to see if they arrive at a consistent result. In our cavity clearing scenario of Section 4.1 we estimated a mass of ~ 2 $M_\odot$ in the ridge. From our observations in Section 3.5 we estimated a dust mass of $\sim 6\times10^{-4}$ $M_\odot$. Using a representative gas-to-dust mass ratio of $R \sim 10^4$, inferred from Table 2, the mass in the ridge is ~ 6 $M_\odot$, and in reasonable agreement with the earlier estimate.

5 CONCLUSIONS

We have obtained 10- and 20-μm broad-band images, 10-μm spectroscopy, and an [S IV] image at 10.5 μm of the central region of RCW 38. The main results from our study are as follows.

(1) Modelling of the emission-line structure at IRS1 indicates that the ionizing radiation field characterizes a star of type O5.5 or O5 with an effective temperature $T_{eff} \simeq 44\,000$ K. The hydrogen number density is $n_H \simeq 10^4$ cm^{-3}.

(2) From fits to the 8–13 μm spectrum of IRS1 we find a dust colour temperature at this point of around 175 K.

(3) A dust temperature map is produced from the *N*- and *Q*-band continuum images and shows the ridge of emission, of which IRS1 is a part, to have a relatively uniform temperature structure, with an average of around 160 K. However, there are a number of peaks in the dust temperature, up to 175 K, which correspond well with the intensity peaks in the *N*- and *Q*-band images. One of these peaks is situated at IRS1.

(4) From the temperature and continuum emission images we are able to derive an opacity map which shows material collecting at the western, or outer, edge of the ridge, which itself forms part of a shell around IRS2.

(5) We have proposed that the region can be explained in terms of a wind-blown cavity, where the stellar wind from the hot young star in IRS2 has cleared a cavity about itself, and the ridge of emission we observe at IRS1 then represents the material which has been swept up into a shell around IRS2.

(6) Modelling the effects of direct heating on the dust shell predicts a large temperature gradient across the shell (50 K from inner to outer edges). We do not, however, see such a gradient in our temperature maps, indicating that this form of heating certainly does not dominate the region.

(7) We have estimated the heating effect of the Lyα photons on the dust, and conclude that if the gas density is $n_H = 10^4$ cm^{-3}, as at IRS1, then silicate-type dust would reach an equilibrium temperature around 175 K if the gas-to-dust mass ratio R is of the order of several times 10^4. A significant dust depletion over normal interstellar values is therefore required.

(8) We estimate the mass of dust in the ridge around IRS1 to be about 5.7×10^{-4} $M_\odot$, and if we take a gas-to-dust mass ratio of around 10^4:1, we find a total mass in the ridge of at least 5.7 $M_\odot$ of gas and dust. This mass estimate is reasonably consistent with a mass estimate of the shell (2 $M_\odot$) derived from modelling the expanding cavity driven by the stellar wind.

(9) An image in the [S IV] fine-structure line at 10.51 μm shows structure whose large scale is similar to that of the dust emission, but whose peaks do not exactly coincide with the continuum emission or temperature distribution peaks.

ACKNOWLEDGMENTS

CHS is supported by an Australian Research Council Senior Research Fellowship. TLB acknowledges financial support from an SAO Predoctoral Fellowship. DKA acknowledges with thanks the support of a Leverhulme Trust Grant, a Visiting Professorship with University College, ADFA, and the use of facilities at the University of York and Royal Observatory Edinburgh. JWVS thanks the Alexander von Humbolt Foundation and the Australian Department of Industry, Science and Tourism for support. We thank ESO and ATAC for the award of observing time, and the staff of the ESO 2.2-m telescope and the AAT for their cheerful assistance. We also thank Ted Bergin for data in advance of publication. Finally, we thank Drs Toby Moore, Torsten Böker, Alfred Krabbe, Carsten Dominik, Michiel Hogerheijde, Aigen Li and Gerd Jan van Zadelhoff for valuable discussions and assistance.

REFERENCES

Aitken D. K., Jones B., 1973, ApJ, 184, 127
Aitken D. K., Griffiths J., Jones B., 1977, MNRAS, 179, 179
Aitken D. K., Bailey A. J., Roche P. F., Hough J. H., 1985, MNRAS, 215, 425

Allen D., Meadows V, 1992, Astronomy, 20, 38
Axon D. J., Ellis R. S., 1976, MNRAS, 177, 499
Baldwin J., Ferland G. J., Martin P. G., Corbin M., Cota S., Peterson B. M., Slettebak A., 1991, ApJ, 374, 580
Beck S. C., Fischer J., Smith H. A., 1991, ApJ, 383, 336
Bodenheimer P., Tenorio-Tagle B., Yorke H. W., 1979, ApJ, 233, 85
Böker T., Storey J. W. V., Krabbe A., Lehmann T., 1997, PASP, 109, 827
Cheung L. H., Frogel J. A., Gezari D. Y., Hauser M. G., 1980, ApJ, 240, 74
Chini R., Kruegal E., Kreysa E., 1986, A&A, 167, 315
Colgan S. W. J., Simpson J. P., Rubin R. J., Erickson E. F., Haas M. R., Wold J., 1991 ApJ, 366, 172
Danziger I. J., 1974, ApJ, 193, 69
Davis L., Greenstein J. L., 1951, ApJ, 114, 206
Day K. L., 1979, ApJ, 234, 158
Dorschner J., Friedemann C., Gürtler J., Henning T., 1988, A&A, 198, 223
Doyon R., Puxley P. J., Joseph R. D., 1992, ApJ, 397, 117
Draine B. T., Lee H. M., 1984, ApJ, 285, 89
Epchtein N., Turon P., 1979, A&A, 72, L4
Ferland G. J., 1993, Dept. of Physics and Astronomy Internal Report, Univ. Kentucky
Frogel J. A., Persson S. E., 1974, ApJ, 192, 351 (FP74)
Fujiyoshi T., Smith C. H., Moore T. J. T., Aitken D. K., Roche P. F., Quinn D. E., 1998, MNRAS, 296, 225
Furniss I., Jennings R. E., Moorwood A. F. M., 1975, ApJ, 202, 400
Genzel R. G., 1993, in Pfenniger D., Bartholdi P., eds, The Galactic Interstellar Medium. Saas–Fee Advanced Course 21, Springer–Verlag, Heidelberg, pp. 275–391
Gillespie A. R., White G. J., Watt G. D., 1979, MNRAS, 186, 383
Gillett F. C., Forrest W. J., Merrill K. M., Capps R. W., Soifer B. T., 1975, ApJ, 200, 609
Goss W. M., Shaver P. A., 1970, Aust. J. Phys. Suppl., 14, 1
Gum C. S., 1952, Observatory, 72, 151
Gum C. S., 1956, Observatory, 76, 150
Hackwell J. A., Gehrz R. D., Smith J. R., Briotta D. A., 1978, ApJ, 221, 797
Hanson M. M., Howarth I. D., Conti P. S., 1997, ApJ, 489, 698
Hoare M. G., Roche P. F., Glencross W. M., 1991, MNRAS, 251, 584
Jäger C., Mutschke H., Begemann B., Dorschner J., Henning Th., 1994, A&A, 292, 641
Klare G., Neckel Th., 1977, A&AS, 27, 215
Kuiper T. B. H., Whiteoak J. B., Fowler J. W., Rice W., 1987, MNRAS, 227, 1013
Kurucz R. L., 1994, Smithsonian Astrophysical Observatory, Kurucz CD–ROM No. 19
Lacy J. H., Beck S. C., Geballe T. R., 1982, ApJ, 255, 510
Lamers H. J., Snow T. P., Lindholme D. M., 1995, ApJ, 455, 269
Lang K. R., 1992, Astrophysical Data: Planets and Stars, Springer-Verlag, New York
Lester D. F., Dinerstein H. L., Rank D. M., 1979, ApJ, 229, 981
Leung C. M., 1975, ApJ, 199, 340
Leung C. M., 1976 J. Quant. Spectrosc. Radiat. Transfer, 16, 559
Li A., Greenberg J. M., 1997, A&A, 323, 566
Ligori S., Moneti A., Robberto M., Guarnieri M. D., Zinnecker H., 1994, Mem. Soc. Astron. Ital., 65, 815
Lumsden S. L., Puxley P. J., 1996, MNRAS, 281, 493
Martin P. G., 1978, Cosmic Dust. Oxford Univ. Press, Oxford
Mathews W. G., 1969, ApJ, 157, 583
Mathis J. S., Rumpl W., Nordsieck K. H., 1977, ApJ, 217, 425
Mitchell R. M., Robinson G., 1978, ApJ, 220, 841
Mitchell R. M., Robinson G., 1980, MNRAS, 190, 669
Mizutani K., Suto H., Takami H., Maihara T., Sood R. K., Thomas J. A., Shibai H., Okuda H., 1987, MNRAS, 228, 721
Muzzio J. C., 1979, AJ, 84, 639
Natta A., Panagia N., 1976, A&A, 50, 191
Panagia N., 1973, AJ, 78, 929
Panagia N., 1975, A&A, 42, 139
Penman J. M., 1976, MNRAS, 175, 149
Persson S. E., Frogel J. A., Aaronson M., 1976, ApJ, 208, 753
Radhakrishnan V., Goss W. M., Murray J. D., Brook J. W., 1972, ApJS, 24, 49
Rank D. M., Dinerstein H. L., Lester D. F., Bregman J. D., Aitken D. K., Jones B., 1978, MNRAS, 185, 179
Robinson G., Smith R. G., Hyland A. R., 1992, MNRAS, 256, 437
Roche P. F., Aitken D. K., 1984, MNRAS, 208, 481
Rodgers A. W., Campbell C. T., Whiteoak J. B., 1960, MNRAS, 121, 123
Scott A., Duley W. W., 1996, ApJS, 105, 401
Shields J. C., 1993, ApJ, 419, 181
Simpson J. P., Rubin R. H., 1984, ApJ, 281, 184
Simpson J. P., Colgan S. W. J., Rubin R. H., Erickson E. F., Haas M. R., 1995, in Haas M. R., Davidson J. A., Erickson E. F., eds, ASP Conf. Ser. Vol. 73, Airborne Astronomy Symposium on the Galactic Ecosystem. Astron Soc. Pac., San Francisco, p. 53
Spitzer L., 1978, Physical Processes in the Interstellar Medium, Wiley, New York
Storey J. W. V., Bailey J., 1982, Publ. Astron. Soc. Aust., 4, 430
Takami H. et al., 1987, PASP, 99, 832
Tielens A. G. G. M., de Jong T., 1979, A&A, 75, 326
White G. J., Phillips J. P., 1983, MNRAS, 202, 255
Wright C. M., 1994, PhD thesis, Univ. New South Wales
Wright E. L., 1973, ApJ, 185, 569
Zinchenko I., Mattila K., Toriseva M., 1995, A&AS, 111, 95

This paper has been typeset from a TEX/LATEX file prepared by the author.